



Titre: A three-dimensional discontinuous galerkin time-domain finite element method for electromagnetic modeling of wireless power transfer coils
Title:

Auteurs: Bita Arabsalmanabadi, Homa Arab, Victor H. G. Amador, Steven Dufour, & Kamal Al-Haddad
Authors:

Date: 2021

Type: Article de revue / Article


Référence: Arabsalmanabadi, B., Arab, H., Amador, V. H. G., Dufour, S., & Al-Haddad, K. (2021). A three-dimensional discontinuous galerkin time-domain finite element method for electromagnetic modeling of wireless power transfer coils. IEEE Open Journal of the Industrial Electronics Society, 2, 360-371.
Citation: <https://doi.org/10.1109/ojies.2021.3077389>

 **Document en libre accès dans PolyPublie**
Open Access document in PolyPublie

URL de PolyPublie: <https://publications.polymtl.ca/9336/>
PolyPublie URL:

Version: Version officielle de l'éditeur / Published version
Révisé par les pairs / Refereed

Conditions d'utilisation: CC BY
Terms of Use:

 **Document publié chez l'éditeur officiel**
Document issued by the official publisher

Titre de la revue: IEEE Open Journal of the Industrial Electronics Society (vol. 2)
Journal Title:

Maison d'édition: IEEE
Publisher:

URL officiel: <https://doi.org/10.1109/ojies.2021.3077389>
Official URL:

Mention légale: This work is licensed under a Creative Commons Attribution 4.0 License. For more information, see <https://creativecommons.org/licenses/by/4.0/>
Legal notice:

A Three-Dimensional Discontinuous Galerkin Time-Domain Finite Element Method for Electromagnetic Modeling of Wireless Power Transfer Coils

BITA ARABSALMANABADI ¹ (Student Member, IEEE), HOMA ARAB ² (Member, IEEE), VICTOR H. AMADOR G. ¹ (Student Member, IEEE), STEVEN DUFOUR ² (Member, IEEE), AND KAMAL AL-HADDAD ¹ (Fellow, IEEE)

¹ Département De Génie Électrique, École De Technologie Supérieure, Montréal H3C 1K3, Canada

² Département De Mathématiques Et De Génie Industriel, Polytechnique Montréal, Montréal H3T 1J4, Canada

CORRESPONDING AUTHOR: BITA ARABSALMANABADI (e-mail: bita.arabsalmanabadi.1@ens.etsmtl.ca).

ABSTRACT Inductive coupling based wireless power transfer (WPT) is a popular short-range power delivery mechanism for many industrial, biomedical, and home electronic appliances applications. A numerical methodology is needed for the analysis of the electromagnetic propagation, radiation, scattering and coupling of highly efficient WPT systems. This study is based on the discontinuous Galerkin time-domain (DGTD) finite element method. A brief survey of the DGTD method is given, which is a finite element method using discontinuous piecewise polynomials as basis functions and numerical fluxes based on up-winding for stability. DGTD method is characterized by the fact that no continuity is enforced between the elements, then it is easy to parallelize and results in fast solvers. Even though the finite element method is used by a few researchers to study WPT problems, we found no study using the DGTD method to study WPT problems, which is surprising given that this discretization technique seems particularly well suited for these problems. A design of two coils at the frequency of 3 MHz is introduced, and the effects of the distance and misalignment between two coils on the mutual coupling are studied. The numerical results are validated by experimental and analytical results.

INDEX TERMS Coils, computational modeling, discontinuous Galarkin method, electromagnetic propagation, finite element analysis, mathematical model, Maxwell equations, mutual inductance, numerical analysis, time-domain analysis, wireless power transfer.

NOMENCLATURE

n	Outward pointing normal vector.
\mathbf{H}	Magnetic field.
\mathbf{E}	Electric field.
ω	Angular frequency.
σ	Conductivity.
ε	Permittivity.
μ	Permeability.
\sim	Normalized value.
Ω	Bounded domain.

Ω_h	Computational domain.
ρ_s	Surface charge density.
J_s	Surface current density.
K	Number of elements.
v, w	Test functions.
\mathbb{M}	Mass matrix.
\mathbb{S}	Stiffness matrix.
M	Mutual inductance.
d	Vertical distance between two coils.
r_1, r_2	Radius of primary and secondary coil.

ϕ_1, ϕ_2	Angle of arbitrary points from x-axis.
r	Distance between two arbitrary points.
$d\ell_1, d\ell_2$	Differential length on primary and secondary coil.
N_1, N_2	Number of turns in the primary and secondary coil.
m_1, m_2, m_3	Longitudinal, lateral, vertical misalignment.
R	Transformation matrix.
$R_{translation}$	Translation matrix.
$R_{rotation}$	Rotation matrix.
δ, θ, α	Clockwise rotation around x, y, and z-axis.

I. INTRODUCTION

Wireless power transmission (WPT) has experienced tremendous progress in the past two decades. The WPT technology can be applied in various fields including transportation, home appliances, biomedical, consumer electronics, and electric vehicles [1]–[5]. However, WPT is plagued by low efficiency, which is related to many factors. The orientation and the misalignment between the transmitter (TX) and the receiver (RX) coils are the two main factors that decrease WPT operation efficiency. Using multiple coils or metamaterial components makes it possible to design systems that can efficiently adapt to magnetic field propagation conditions [6]–[12]. Their design can therefore be complex. To solve this problem, the whole radiation characteristic needs to be modeled and measured in order for the designed WPT system to operate correctly. But the possibilities are practically limitless. A trial and error approach is therefore not practical. Optimization techniques must therefore be used to automate the obtention of optimal designs.

A numerical methodology for the discretization of full-wave Maxwell's equations in the time domain that is accurate, fast and robust is needed for the analysis of the electromagnetic propagation, radiation, scattering and coupling of highly efficient WPT systems. Various commercial codes like ANSYS, COMSOL, ADS are available to perform such studies [13]–[15]. They are mainly based on finite element methods and they are particularly designed to study either low frequency or high frequency problems.

In [16], authors have correctly mentioned about the gap between low and high frequencies as conventional low frequency methods cannot include displacement current, while common high frequency methods focus mainly on the ultrahigh frequencies, such as in antenna studies. In fact, the frequency range in which WPT systems can vary is large and could be in both frequency intervals, depending on the application and on operating conditions. Most commercial software are based on a simplified version of Maxwell's equations or on electromagnetic scattering models which are formulated in the frequency domain. They require little computational resources and they have good solution convergence but they neglect important physics that can only be modeled using full-wave Maxwell's equations. For example, Helmholtz equation

is a frequency-domain method used to analyze wave propagation in high frequency range [17]. The H-form is used mainly in low frequency, and it neglects displacement current or magnetic induction [18]. Integral methods are based on an integral form of Maxwell's equations and only the boundaries need to be discretized. This approach reduces the number of degrees of freedom and it is known to give good accuracy for some problems. But they do not perform well when dealing with complex materials and geometries.

Methods based on partial differential equations can be applied on the whole structure of the problem. Differential equations can be expressed in the frequency domain (FD) or in the time domain (TD). FD methods are often computationally inefficient for wideband frequency responses since, for a single frequency, the simulation has to be run completely. The finite difference time-domain (FDTD) method is used in many commercial software. It is known to give inaccurate results on complex geometries [19], [20]. The Galerkin time-domain (GTD) finite element method is popular for its accuracy when dealing with large and complex structures [21]. But since the interpolation functions must be continuous across elements, multimaterial problems cannot be modeled accurately. Closed-source commercial codes also make it difficult to use optimization techniques. They are often too slow to repeat the simulations for a large number of parameters.

In this work, DGTD FEM is used for modeling WPT systems based on three-dimensional full-wave Maxwell's equations. The proposed formulation is based on an upwind numerical flux, Whitney basis expansions on a tetrahedron (3D case) and a Runge-Kutta time stepping scheme. The DGTD FEM exhibits better convergence and stability properties when compared to the standard FEM [22], [23]. Open-source software gives us the flexibility to apply gradient-based optimization methods inside various sections of a code. It is therefore easier to control the key parameters during a simulation and to use parallel computing techniques for these specific problems.

This paper is organized as follows: In Section II, numerical and analytical equations are presented to calculate the electromagnetic fields and mutual inductance between two rings when either their axes are aligned or have lateral and angular misalignments. A time domain 3-D DGTD solver is developed to discretize the full wave Maxwell's equations. A theoretical analysis of coupling effects in WPT coil systems has been presented with elliptic integrals, and the formulas for mutual inductance have been derived. In Section III, the numerical results of the electromagnetic fields of one and two rings are presented and compared with their corresponding experimental and analytical results. In addition, a comparison is made between the experimental and numerical results of the WPT as the geometrical parameters are varied. Finally, we conclude our work in Section IV. The comparison shows that the proposed numerical method has high accuracy and computational efficiency, which would provide some guides for the design and optimization of coils in WPT.

II. FORMULATIONS

A. NUMERICAL METHODOLOGY

In differential form, Maxwell’s equations in free space, on a bounded domain $\Omega \subset \mathbb{R}^3$, are given by:

$$\begin{aligned} \mu \frac{\partial \mathbf{H}}{\partial t} + \nabla \times \mathbf{E} &= \mathbf{0} \\ \nabla \cdot \mathbf{E} &= 0 \\ \varepsilon \frac{\partial \mathbf{E}}{\partial t} - \nabla \times \mathbf{H} &= \mathbf{0} \\ \nabla \cdot \mathbf{H} &= 0 \end{aligned} \tag{1}$$

where \mathbf{E} is the electric field, \mathbf{H} is the magnetic field, μ is the permeability, and ε represents the permittivity of the material. Appropriate initial and boundary conditions complete the definition of the problem. In order for a boundary value problem to be well-posed, appropriate boundary conditions must be prescribed on the boundary $\Gamma = \partial\Omega$ of the domain. For Maxwell’s equations, depending on the problem under study, boundary conditions can be of the form:

$$\begin{aligned} \mathbf{n} \cdot (\mathbf{E}_1 - \mathbf{E}_2) &= \rho_s \quad (\text{Dirichlet}) \\ \mathbf{n} \times (\mathbf{E}_1 - \mathbf{E}_2) &= 0 \quad (\text{Neumann}) \end{aligned} \tag{2}$$

for the electric field \mathbf{E} in media 1 and 2, and of the form:

$$\begin{aligned} \mathbf{n} \cdot (\mathbf{H}_1 - \mathbf{H}_2) &= 0 \quad (\text{Dirichlet}) \\ \mathbf{n} \times (\mathbf{H}_1 - \mathbf{H}_2) &= \mathbf{J}_s \quad (\text{Neumann}) \end{aligned} \tag{3}$$

for the magnetic field \mathbf{H} in media 1 and 2, where \mathbf{n} is the unit outward pointing normal vector, ρ_s is surface charge density, and \mathbf{J}_s is surface current density. We assume the physical domain Ω is approximated by the computational domain Ω_h using tetrahedral elements as

$$\Omega_h = \cup_K D_K \tag{4}$$

where our domain is approximated by the union of K non overlapping elements, D_K . Let’s now consider one of those tetrahedral elements of Ω_h . The weak form is used to turn the differential equation associated with the first and third equations of system (1) into an integral equation [24]. In order to obtain the elementary weak form, we first multiply by test functions \mathbf{v} and \mathbf{w} taken in an appropriate functional space, and we integrate over D to obtain

$$\begin{aligned} \int_D \partial_t(\mu \mathbf{H}) \cdot \mathbf{v} \, d\mathbf{x} + \int_D (\nabla \times \mathbf{E}) \cdot \mathbf{v} \, d\mathbf{x} &= 0 \\ \int_D \partial_t(\varepsilon \mathbf{E}) \cdot \mathbf{w} \, d\mathbf{x} - \int_D (\nabla \times \mathbf{H}) \cdot \mathbf{w} \, d\mathbf{x} &= 0 \end{aligned} \tag{5}$$

Using the vectorial identity

$$\begin{aligned} \nabla \cdot (\mathbf{a} \times \mathbf{b}) &= \mathbf{b} \cdot \nabla \times \mathbf{a} - \mathbf{a} \cdot \nabla \times \mathbf{b} \\ &= (\nabla \times \mathbf{a}) \cdot \mathbf{b} - \mathbf{a} \cdot (\nabla \times \mathbf{b}) \end{aligned} \tag{6}$$

with the divergence theorem

$$\int_D \nabla \cdot (\mathbf{a} \times \mathbf{b}) \, d\mathbf{x} = \int_{\partial D} (\mathbf{a} \times \mathbf{b}) \cdot \mathbf{n} \, d\mathbf{s} \tag{7}$$

where ∂D is the boundary of element K , we get the “integration by parts” formula

$$\begin{aligned} \int_D (\nabla \times \mathbf{a}) \cdot \mathbf{b} \, d\mathbf{x} &= \int_D \mathbf{a} \cdot (\nabla \times \mathbf{b}) \, d\mathbf{x} + \int_{\partial D} (\mathbf{a} \times \mathbf{b}) \cdot \mathbf{n} \, d\mathbf{s} \end{aligned} \tag{8}$$

which is first applied to the non-transient term of the first equation of system (1) to give

$$\begin{aligned} \int_D (\nabla \times \mathbf{E}) \cdot \mathbf{v} \, d\mathbf{x} &= \int_D \mathbf{E} \cdot (\nabla \times \mathbf{v}) \, d\mathbf{x} + \int_{\partial D} (\mathbf{E} \times \mathbf{v}) \cdot \mathbf{n} \, d\mathbf{s} \\ &\approx \int_D \mathbf{E} \cdot (\nabla \times \mathbf{v}) \, d\mathbf{x} + \int_{\partial D} (\mathbf{n} \times \mathbf{E}^*) \cdot \mathbf{v} \, d\mathbf{s} \end{aligned} \tag{9}$$

where the vectorial identity $(\mathbf{b} \times \mathbf{c}) \cdot \mathbf{a} = (\mathbf{a} \times \mathbf{b}) \cdot \mathbf{c}$ was used in the boundary term. Also, since the value of \mathbf{E} on ∂D also depends on the contributions of the neighboring elements, an approximation $\mathbf{E} \approx \mathbf{E}^*$ is used, where \mathbf{E}^* will be provided by a “numerical model” to be determined. We then apply formula (7) a second time to the previous expression to get

$$\begin{aligned} \int_D \mathbf{E} \cdot (\nabla \times \mathbf{v}) \, d\mathbf{x} + \int_{\partial D} (\mathbf{n} \times \mathbf{E}^*) \cdot \mathbf{v} \, d\mathbf{s} &= \\ \int_D (\nabla \times \mathbf{E}) \cdot \mathbf{v} \, d\mathbf{x} - \int_{\partial D} (\mathbf{n} \times \mathbf{E}) \cdot \mathbf{v} \, d\mathbf{s} + \int_{\partial D} (\mathbf{n} \times \mathbf{E}^*) \cdot \mathbf{v} \, d\mathbf{s} &= \\ \int_D (\nabla \times \mathbf{E}) \cdot \mathbf{v} \, d\mathbf{x} - \int_{\partial D} [\mathbf{n} \times (\mathbf{E} - \mathbf{E}^*)] \cdot \mathbf{v} \, d\mathbf{s} \end{aligned} \tag{10}$$

where the above vectorial identity was again used. This finally gives us the weak form associated with the first equation of system (5)

$$\begin{aligned} \int_D \partial_t(\mu \mathbf{H}) \cdot \mathbf{v} \, d\mathbf{x} + \int_D (\nabla \times \mathbf{E}) \cdot \mathbf{v} \, d\mathbf{x} &= \\ \approx \int_{\partial D} [\mathbf{n} \times (\mathbf{E} - \mathbf{E}^*)] \cdot \mathbf{v} \, d\mathbf{s} \end{aligned} \tag{11}$$

We proceed in a similar way to get the weak form for the second equation of system (5)

$$\begin{aligned} \int_D \partial_t(\varepsilon \mathbf{E}) \cdot \mathbf{w} \, d\mathbf{x} - \int_D (\nabla \times \mathbf{H}) \cdot \mathbf{w} \, d\mathbf{x} &= \\ \approx - \int_{\partial D} [\mathbf{n} \times (\mathbf{H} - \mathbf{H}^*)] \cdot \mathbf{w} \, d\mathbf{s} \end{aligned} \tag{12}$$

The mass \mathbb{M} and stiffness \mathbb{S} matrices can be defined as

$$\begin{aligned} \mathbb{M} &= \int_D \mathbf{v} \cdot \mathbf{w} \, d\mathbf{x} \\ \mathbb{S} &= \int_D \mathbf{v} \cdot (\nabla \times \mathbf{w}) \, d\mathbf{x} \end{aligned} \tag{13}$$

The base functional space associated with these weak forms is expressed as

$$H(\text{curl}; \Omega) = \{ \mathbf{u} \in [L^2(\Omega)]^3 \mid \nabla \times \mathbf{u} \in [L^2(\Omega)]^3 \} \tag{14}$$

which is a variation of the $H^1(\Omega)$ Sobolev space used with classical finite element formulations, where $L^2(\Omega)$ is the set of square-integrable functions [25], [26].

The discrete finite element approximations $\mathbf{E}_h \approx \mathbf{E}$ and $\mathbf{H}_h \approx \mathbf{H}$ will belong to a discrete functional subspace $U_h \subset H(\text{curl}; \Omega)$. Discrete test functions \mathbf{v}_h and \mathbf{w}_h will also be taken in U_h . We will not repeat the arguments here but refer to [24] for the details. The classical approach consists in using nodal approximations of the form

$$\begin{aligned} \mathbf{E}_h &= \sum_{N=1}^4 E_N \mathbf{v}_N \\ \mathbf{H}_h &= \sum_{N=1}^4 H_N \mathbf{w}_N \end{aligned} \quad (15)$$

where the E_N and H_N are scalar degrees of freedom of a give tetrahedral element D . Even though this approach works in many situations, nodal approximations are known to be unstable for some problems. This bring us to use vectorial approximations where we replace the scalar degrees of freedom by vectorial degrees of freedom \mathbf{E}_N and \mathbf{H}_N . Whitney element, also known as an edge element, is a popular discrete subspace function for the discretization of Maxwell's equations. In this method, six shape functions are associated with each three-dimensional tetrahedral element [27].

The boundary terms $-\mathbf{n} \times \mathbf{E}^*$ and $\mathbf{n} \times \mathbf{H}^*$ in the weak forms of the equations of system (5) contain the so called fluxes. To complete the scheme, the solution on each edge of two neighbor elements must be connected. There are several possible choices of this flux function here we choose the up-winding flux given by [24]

$$\begin{aligned} &-\mathbf{n} \times (\mathbf{E} - \mathbf{E}^*) \\ &= \frac{1}{2}(\mathbf{n} \times \|\mathbf{E}_N^h\| - \|\mathbf{H}_N^h\| + (\mathbf{n} \cdot \|\mathbf{H}_N^h\|) \mathbf{n}) \\ &\mathbf{n} \times (\mathbf{H}_N - \mathbf{H}_N^*) \\ &= \frac{1}{2}(-\mathbf{n} \times \|\mathbf{H}_N^h\| - \|\mathbf{E}_N^h\| + (\mathbf{n} \cdot \|\mathbf{E}_N^h\|) \mathbf{n}) \end{aligned} \quad (16)$$

where $\|\mathbf{u}\| = \mathbf{n} \cdot \mathbf{u}^+ - \mathbf{n} \cdot \mathbf{u}^-$ with a superscript “-” refer to the interior information of the element and a superscript “+” refer to the exterior information.

Backward differentiation formulas (BDF) time integration schemes is considered for the approximation of the time derivative in maxwell's equations. It is an implicit methods Lagrange interpolation polynomial for the numerical integration of ordinary differential equations [28]. Using higher order BDF schemes does not result in significant accuracy improvements when compared to the second-order accurate scheme [29].

The matrix obtained from numerical methods is in ill-conditions because of the magnitude of the different parameters. Therefore, for reducing the round-off errors and ill-conditioned problems the non-dimensional variables are

TABLE I Normalization System of Equations

Normalization if $\sigma \ll \omega\epsilon$	
$\Pi_1 \tilde{\mu} \frac{\partial \tilde{\mathbf{H}}}{\partial \tilde{t}} + \tilde{\nabla} \times \tilde{\mathbf{E}} = 0$	$\Pi_1 = \frac{\mu_0 H_0 l_0}{t_0 E_0}$
$\tilde{\nabla} \cdot \tilde{\mathbf{H}} = 0$	
$\Pi_2 \tilde{\epsilon} \frac{\partial \tilde{\mathbf{E}}}{\partial \tilde{t}} - \tilde{\nabla} \times \tilde{\mathbf{H}} = 0$	$\Pi_2 = \frac{\epsilon_0 E_0 l_0}{t_0 H_0}$
$\tilde{\nabla} \cdot \tilde{\mathbf{E}} = 0$	
Normalization if $\sigma \gg \omega\epsilon$	
$\Pi_1 \tilde{\mu} \frac{\partial \tilde{\mathbf{H}}}{\partial \tilde{t}} + \tilde{\nabla} \times \tilde{\mathbf{E}} = 0$	$\Pi_1 = \frac{\mu_0 H_0 l_0}{t_0 E_0}$
$\tilde{\nabla} \cdot \tilde{\mathbf{H}} = 0$	
$\Pi_3 \tilde{\rho} \tilde{\nabla} \times \tilde{\mathbf{H}} = \tilde{\mathbf{E}}$	$\Pi_3 = \frac{\rho H_0}{t_0 E_0}$
$\tilde{\nabla} \cdot \tilde{\mathbf{E}} = 0$	

considered. The normalized system of equations are presented in Table I.

In the case of $\sigma \ll \omega\epsilon$, the unit-free variables are defined as: $\tilde{\mathbf{H}} = \mathbf{H}/H_0$ where H_0 is a unit magnetic field strength, $\tilde{\mathbf{E}} = \mathbf{E}/E_0$ where E_0 is $H_0 \times Z_0$ with $Z_0 = 120\pi$, and $\tilde{\mu} = \mu/\mu_0$ where μ_0 is $4\pi \times 10^{-7}$, $\tilde{\epsilon} = \epsilon/\epsilon_0$ where ϵ_0 is 8.85×10^{-12} , $\tilde{\nabla} = \nabla/l_0$, $\partial/\partial \tilde{t} = 1/t_0 \partial/\partial t$.

In the case of $\sigma \gg \omega\epsilon$, the unit-free variables are defined as: H_0 is $(4\pi)^{-1} \times 10^7$, $\tilde{\mathbf{E}} = \mathbf{E}/E_0$ where E_0 is a unit electric field strength, and $\tilde{\mu} = \mu/\mu_0$ where μ_0 is $4\pi \times 10^{-7}$, $\tilde{\rho} = \rho/\rho_0$ where ρ_0 is 1.68×10^{-8} , $\tilde{\nabla} = \nabla/l_0$, $\partial/\partial \tilde{t} = 1/t_0 \partial/\partial t$. For simplicity, the \sim symbol is removed from normalized parameters in the following sections.

III. ANALYTICAL METHODOLOGY

The analytical calculation of mutual inductance between two coaxial circular coils has been quite thoroughly assessed by a number of authors since the time of Maxwell [30]. Neumann [31], Butterworth [32], Snow [33] and Grover's formulae [34] and Biot-Savart law [35] are the basis of several analytical models [36], [37]. Most of these formulae suffer from the various cases of singularities and slow convergence.

Mutual inductance is an electric parameter that can be computed by several forms expressed over elliptical integrals of the first, the second, and the third kind; Heuman's Lambda function; Bessel functions; and Legendre functions [38], [39]. It has a strong nonlinear dependence on the shapes, orientations and the distance between two coils which needs to be clarified using a precise model. The analytical solutions form magnetic field components based on elliptic integrals around a circular coil are presented in Appendix A.

In this paper, the coils are assumed as two filamentary circular coils (see Fig 2). The main formula for estimating

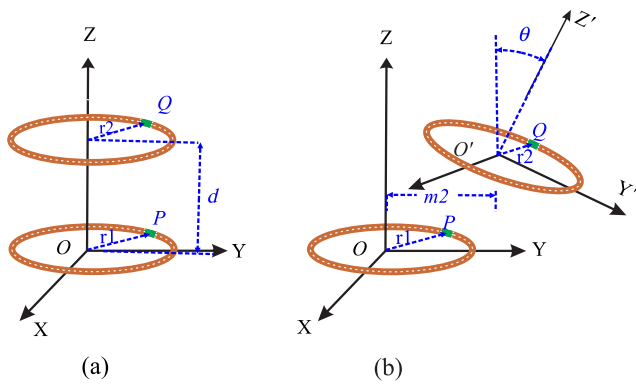


FIG. 1. Two filamentary coils (a) with alignment, and (b) with misalignment.

the mutual inductance between two circular coils is the formula given by Neumann [40], [41] which is employed in this paper. The equations are presented in Cartesian coordinate. By assuming that each conductor carries the constant current density and having constant cross-sectional areas, the mutual inductance is

$$M = \frac{1}{A_1 A_2} \int_{A_2} \int_{A_1} M_{12} dA_1 dA_2 \quad (17)$$

$$M_{12} = \frac{N_1 N_2 \mu_0}{4\pi} \oint_{\ell_1} \oint_{\ell_2} \frac{d\ell_2 d\ell_1}{r} \quad (18)$$

The values of the mutual inductance, with and without alignment, are determined using the Taylor expansion of Neumann’s integral formula presented in [41].

1) ALIGNMENT

Two filamentary circular coaxial coils with radii r_1 and r_2 and the vertical distance of d are presented in Fig 2 a. The center of the primary coil is taken as the origin of Cartesian system $O(0, 0, 0)$. After calculating differential length of conductor elements in arbitrary points of P and Q, and the distance between them (shown in Fig 2 a) and by applying some simplifications, the mutual inductance between two circular coaxial filament coils is (see Appendix B for more details)

$$M = \frac{\mu_0 r_1 r_2}{2\sqrt{r_1^2 + r_2^2 + d^2}} \int_0^{2\pi} \int_0^{2\pi} \frac{\cos(\phi_1 - \phi_2)}{\sqrt{1 - \beta \cos(\phi_1 - \phi_2)}} d\phi_1 d\phi_2 \quad (19)$$

where $\beta = (2r_1 r_2)/(r_1^2 + r_2^2 + d^2)$. Equation (19) has no closed form solution. The Taylor series is used to expand the

denominator of (19). The mutual inductance is then approximated as,

$$M = \frac{\mu_0 \pi \beta \sqrt{r_1 r_2}}{2} \left[1 + \frac{15}{8} \beta^2 + \frac{315}{256} \beta^4 + \dots \right] \quad (20)$$

1) MISALIGNMENT

Numerous literatures have published to present the power energy transformation affected by the location of two inductive coils over the past decades [42]–[44]. However, it still suffers from lack of accurate equations to approximate the effects of noncoaxial coils on the coupling.

In this paper, misalignment situations are presented by coordinate transformation of the secondary coil from the Cartesian coordinate $x'y'z'$ to the Cartesian coordinate xyz . It is assumed that two coils are in two parallel coordinates and by applying the transformation matrix, the secondary coil is transferred to the same coordinate as the primary coil. However, the degree of misalignment is dependent on the nature of the application. For example, in the dynamic electric vehicle charger and medical implant applications, six degrees of freedom misalignment is possible. Figure 1 a, 1 b, and 1 c present the angular misalignment around x , y and z axes, (i.e. pitch, roll, and yaw). Also, Fig 1 d shows the longitudinal, latera, and vertical misalignments along x , y and z axes (i.e. right and left, forward and back, and up and down).

The pitch angle presents a clockwise rotation of θ about the y -axis. θ is the angle between the direction unit vector \mathbf{j} and the directional unit vector of the original \mathbf{j}' reference frame. It is calculated as

$$\theta = \arccos(\mathbf{j} \cdot \mathbf{j}') \quad (21)$$

The transformation matrix which is a combination of translation and rotation matrices are presented as

$$R = [R_{rotation}]d\ell + [R_{translation}] \quad (22)$$

$R_{translation}$ and $R_{rotation}$ are defined as (23) and (24) shown at the bottom this page, respectively.

$$R_{translation} = \begin{bmatrix} m_1 & 0 & 0 \\ 0 & m_2 & 0 \\ 0 & 0 & m_3 - d \end{bmatrix} \quad (23)$$

where m_1, m_2 , and m_3 present the longitudinal, lateral, and vertical misalignments along x, y and z axes. For simplicity, in this paper, the lateral (y -axis translation) and pitch misalignments are considered. By replacing the differential length of conductor elements and the distance between them in (18) (shown in Fig 2 b) and after some simplification, the mutual inductance between two circular non-coaxial filament coils is

$$R_{rotation} = \begin{bmatrix} \cos \alpha \cos \theta & \cos \alpha \sin \theta \sin \delta - \sin \alpha \cos \delta & \cos \alpha \sin \theta \cos \delta + \sin \alpha \sin \delta \\ \sin \alpha \cos \theta & \sin \alpha \sin \theta \sin \delta + \cos \alpha \cos \delta & \sin \alpha \sin \theta \cos \delta - \cos \alpha \sin \delta \\ -\sin \theta & \cos \theta \sin \delta & \cos \theta \cos \delta \end{bmatrix} \quad (24)$$

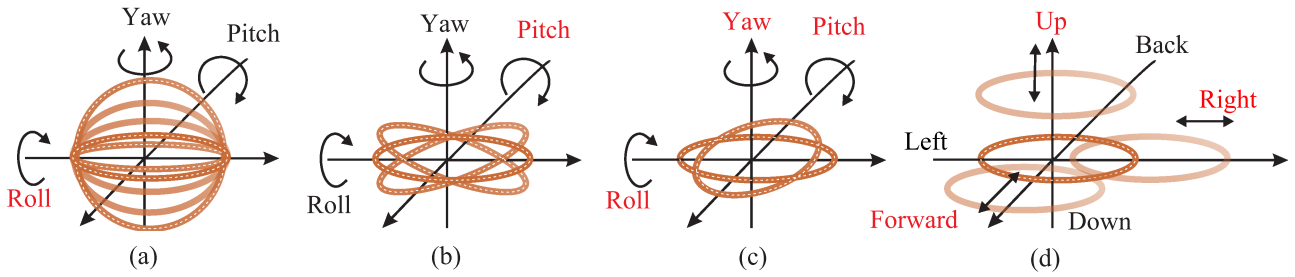


FIG. 2. Rotation and translation misalignments (a) roll, (b) pitch, (c) roll, pitch, and yaw, and (d) up, right and forward translations.

(see Appendix B for more details)

$$M = \frac{\mu_0 r_1 r_2}{2\pi\sqrt{\tau}} \iint \frac{(\sin \phi_1 \sin \phi_2 \cos \theta + \cos \phi_1 \cos \phi_2) d\phi_1 d\phi_2}{\sqrt{1 - (\alpha \cos \phi_1 + \beta \cos \phi_2 + \gamma \cos \phi_1 \cos \phi_2 + \chi \sin \phi_1 \sin \phi_2)}} \quad (25)$$

where $\alpha = 2r_1 m_2 / \tau$, $\beta = (2dr_2 \sin \theta - 2m_2 r_2 \cos \theta) / \tau$, $\gamma = 2r_1 r_2 \cos \theta / \tau$, and $\chi = 2r_1 r_2 / \tau$. The Taylor series is used to expand the denominator of (25) with the fifth order. For simplicity, the higher orders are ignored. Hence, the mutual inductance is

$$M = \frac{\mu_0 \phi r_1^2 r_2^2 \cos \beta}{2\sqrt{\tau^3}} \left[1 + \frac{3\alpha\beta}{4\gamma} + \frac{15}{64}(\gamma^2 + \chi^2 + 4\alpha^2 + 4\beta^2) + \frac{105\alpha\beta}{512\gamma}(11\gamma^2 + 4\alpha^2 + 4\beta^2 + \chi^2) + m5 \right] \quad (26)$$

where

$$m5 = \frac{315}{8192} \left[3\gamma^4 + 3\chi^4 + 24\alpha^4 + 24\beta^4 + 2\gamma^2\chi^2 + 36\gamma^2\alpha^2 + 36\gamma^2\beta^2 + 12\chi^2\alpha^2 + 12\chi^2\beta^2 + 120\alpha^2\beta^2 \right] \quad (27)$$

Equation (27) represents the mutual inductance between two filamentary coils with one turn. For coils with multiple turns, the mutual inductance can be calculated as

$$M_{total} = \sum_{m=1}^M \sum_{n=1}^N M_{m,n} \quad (28)$$

In order to verify the numerical analysis, we use both analytical and experimental analyses which the results are discussed in the following section.

IV. NUMERICAL AND EXPERIMENTAL RESULTS

In this section, the numerical results of WPT coils are shown to verify the capability of the proposed DGTD method. To show the accuracy of the method, the electromagnetic fields around one coil are calculated and compared with analytical

TABLE II Coil Regular and Non-Dimensional Parameters of the Model Evaluation and Applied Boundary Conditions

Parameters	Value	Value normalized
copper wire radius (r)	0.5 cm	0.05 ($l_0 = 0.1$)
coils radius (R)	15 cm	1.5 ($l_0 = 0.1$)
frequency (f)	3 MHz	0.1 ($f_0 = 300$ MHz)
ϵ_0	8.85×10^{-12}	$\Pi_1 = 0.1$
μ_0	$4\pi \times 10^{-7}$	$\Pi_2 = 0.1$
Initial and Dirichlet boundary conditions		
Initial BC	$E_0 = (0, 0, 0)$ $H_0 = (0, 0, 0)$	
Dirichlet BC	$H(x, y, 0, t) = (*, *, \frac{I(\sqrt{x^2+y^2}-R)}{2\pi r^2} \sin(\omega t))$ $E(x, y, z, t) = (*, *, *)$ or free BC	

results. For the mesh decomposition GMSH was used and the area is divided in eight subdomains to apply parallel computation technique [26].

TX, and RX coils are two circular hollow (air core) coils with very thin wall thickness. For simplicity purpose, the study is focused on the electromagnetic field propagation around coils, and uniform current distribution is considered on the boundary of the coils. However, the AC losses and behavior of the electromagnetic field inside coils can be calculated separately to make the simulation faster and more accurate numerically. As an excitation, the z component of the magnetic field is applied on the surface of the coil. The magnetic field on the conductor surface can be defined as

$$\begin{aligned} H(x, t) &= \frac{Ixz}{2\pi r^2 \sqrt{x^2 + y^2}} \sin(\omega t) \\ H(y, t) &= \frac{Iyz}{2\pi r^2 \sqrt{x^2 + y^2}} \sin(\omega t) \\ H(z, t) &= \frac{I(\sqrt{x^2 + y^2} - R)}{2\pi r^2} \sin(\omega t) \end{aligned} \quad (29)$$

Table II shows the parameters of the coil, and applied boundary conditions (BCs). The solution domain is discretized into 562 214 tetrahedra elements. The time step of 0.5×10^{-2} is used, which is the maximum stable time step. The normalization values are chosen as: $H_0 = 1$, $E_0 = 120\pi$, $l_0 = 0.1$, $f_0 = \iota_0^{-1} = 30$ MHz, and $\Pi_1 = \Pi_2 = 0.01$. DGTD model of the coil and computational mesh are depicted in Fig. 3.

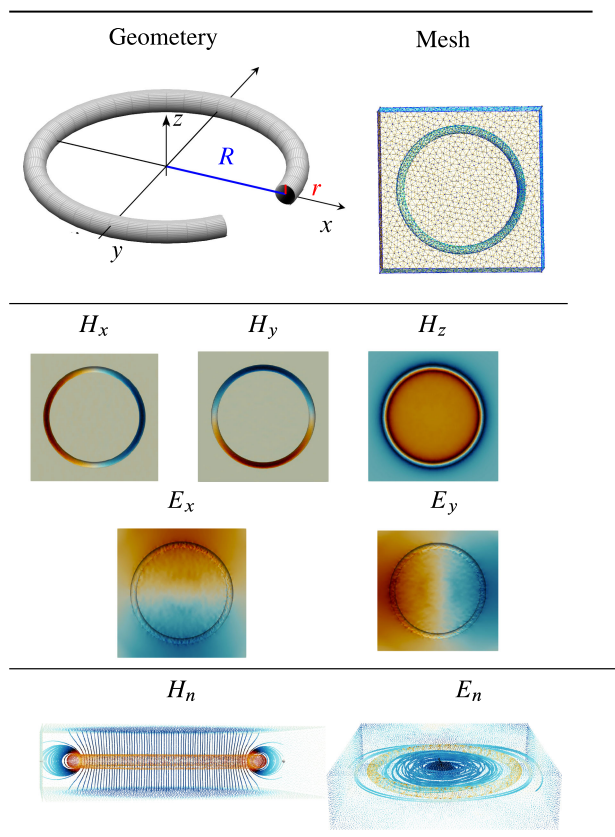


FIG. 3. Geometry, computational mesh, and electromagnetic fields propagation around one coil at 3 MHz. The color scale from blue to red for E is $[-0.25e-2, 0.25e-2]$ and for H is $[-0.5, 0.5]$ at $t = 3.75$

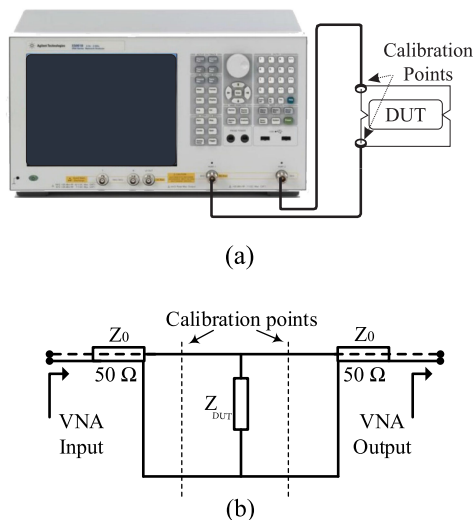


FIG. 4. a) Experimental set-up to measure mutual inductance between TX and RX coils using VNA, b) The circuit for measuring Z_{cut} between two ports of VNA.

The different components of electromagnetic field (H_x, H_y, H_z) and (E_x, E_y) are depicted in Fig. 3. H_n and E_n represent the normalized values of magnetic and electric fields. All the visualizations of this article were produced with paraview [45]. Although DGTD methods are able to

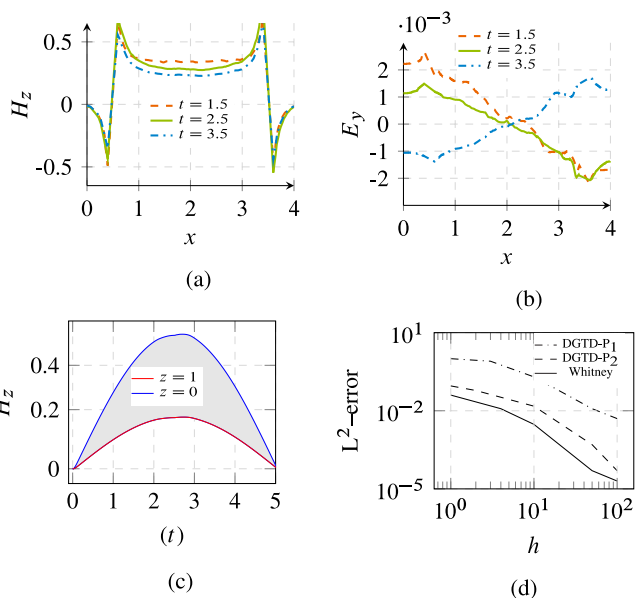


FIG. 5. (a) Magnetic field components along x -axis at various times. (b) Electric field components along x -axis at various times (c) Magnetic field propagation along z -axis. (d) The discrete L^2 -error for magnetic field (H_z) at the center of a circular ring, obtained using DGTD with central fluxes, for different degrees of basis functions

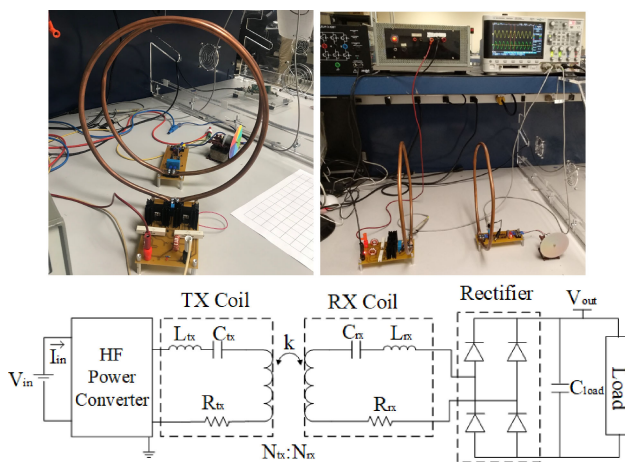


FIG. 6. Measurement set-up and schematic diagram.

reach high orders of accuracy in terms of field interpolation, the 3D visualization of post-processed solutions often lacks the same accuracy, specially for projecting vector solutions to nodal solutions. Figs. 5(a), 5(b) demonstrate the propagation of the electromagnetic fields along the x -axis of the coil. The variation of the magnetic field along z -axis is shown in Fig. 5(c). We define the error between the analytical solution and numerical solution as the norm of the difference between the magnetic field (at $\tilde{z} = 0$ and $\tilde{t} = 2.5$). In Fig. 5(d), the error values are depicted as a function of the maximum edge length (h). In order to measure the influence of the basis order, we show errors calculated for different nodal polynomial orders (P_1, P_2) and Whitney basis functions. A numerical dispersion can be observed when a first order

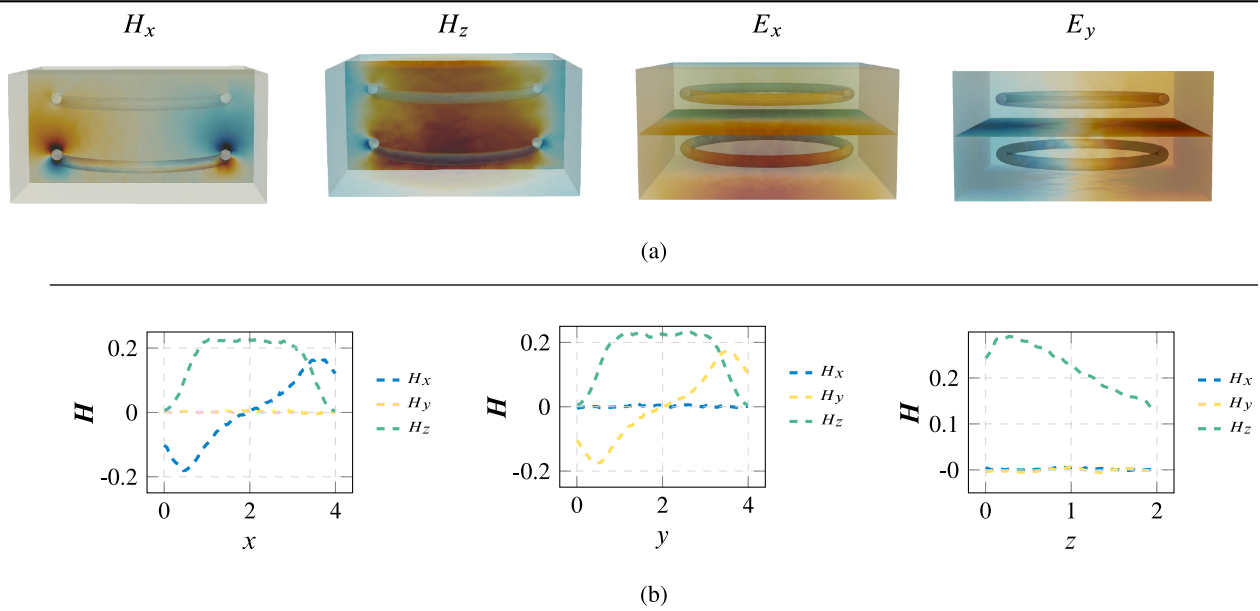


FIG. 7. (a) Distribution of electromagnetic field components around two aligned coils with 10 cm air gap. The color scale from blue to red for E is $[-0.16e-2, 0.16e-2]$, and for H is $[-0.25, 0.25]$ at $t = 2.5$. (b) Magnetic field variation along x , y , and z axis at $t = 2.5$

TABLE III CPU Time and the Memory Overhead to Reach One Period and DoF for Different Basis Functions

	#DoF	%CPU time	%RAM	Time step (Δt)
DGTD-P ₁	562214	63.07	40	0.5×10^{-2}
DGTD-P ₂	1405535	100.00	100	0.5×10^{-2}
DGTD-Whitney	1686642	76.92	120	0.5×10^{-2}

basis function (DGTD-P1) is applied. This dispersion error is not reduced notably by using a finer mesh. On the other hand, the dispersion error is reduced when a second order or Whitney basis functions are used. CPU time and the memory overhead to reach one period of time and DoF for different basis functions are shown in Table III. However, the latter approach requires a large number of degree of freedoms and thus, increases substantially the computing time and memory usage. The method proposed here consist in using a Whitney basis function in the not very fine mesh. As a second case study, a WPT with two coils is studied. The parameters of the two coils TX and RX are chosen as listed in Table II and the vertical distance between two coils is 10 cm. The operating frequency and time-step size are set at 3 MHz and 0.5×10^{-2} , respectively. The solution domain is discretized into 734 014 tetrahedra elements. As a basis function, the Whitney element (edge element) is used due to its divergence free properties.

To verify the DGTD approximations for two coils, a practical setup is built up as shown in Fig. 6. The input voltage and current of the system are 15 V and 10 A, respectively. The DC source feeds the first module of the circuit, which

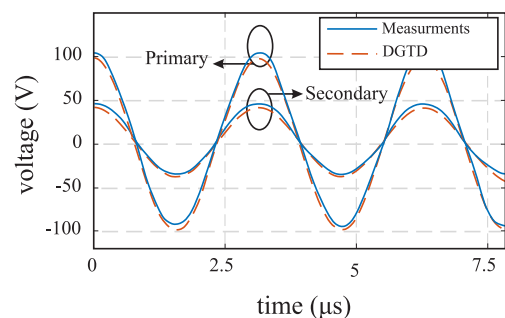


FIG. 8. Measurement and numerical results for voltages in primary and secondary coils at 3 MHz for $d = 10$ cm.

contains a half-bridge which flows through a resonant LC circuit. The gates of the MOSFETs of the half-bridge circuit and the resonant circuit are connected by diodes, thus generating a switching frequency equal to the resonant frequency of the LC resonant circuits. The inductor of this resonant circuit is a single-turn coil with a diameter of 30 cm. The maximum power transfer is at resonant frequency around 3 MHz.

Commercial impedance analyzers like vector network analyzer (VNA), are a commonly used way to measure impedance of passive components especially high-frequency small resistance ones. To measure mutual inductance (M) between two coils, 2-port S-parameter measurements are performed using VNA model E5061B-3L5 LF-RF. VNA is connected to series connected coils (device under test (DUT)) as shown in the Fig. 4. The VNA has a signal generator whose frequency and amplitude can be varied. During the measurement process, the signal with a specific frequency and

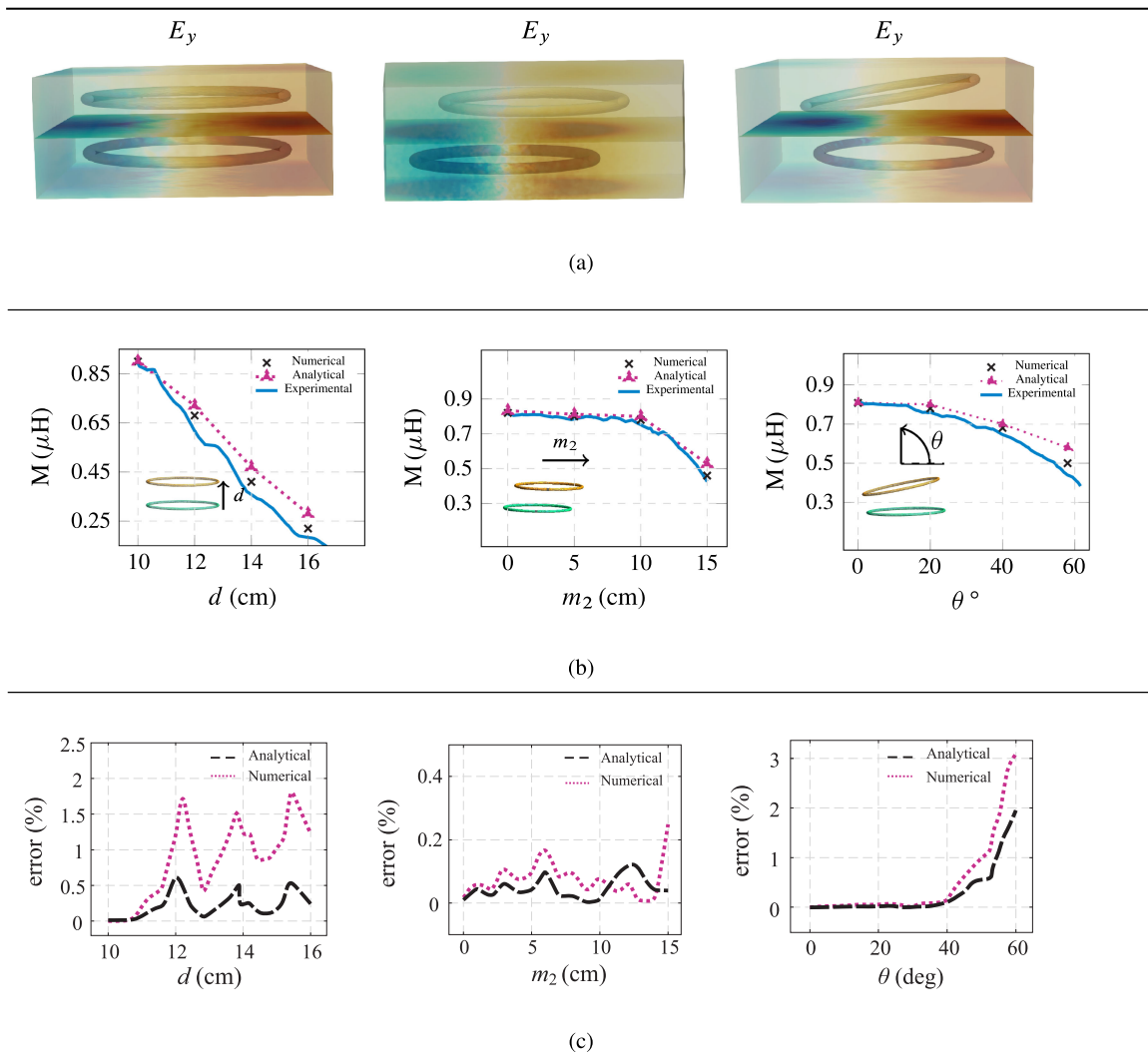


FIG. 9. (a) Effect of misalignment on electric field propagation between two coils. The color scale from blue to red for E is $[-0.25e-2, 0.25e-2]$ at $t = 3.75$. (b) Effect of misalignment on mutual inductance (M) between two coils. (c) Mean square error among numerical and analytical versus experimental results.

amplitude passed through the DUT using one of the ports, while another port was terminated by a 50Ω load. From this information, the VNA generated S-parameters for one of the ports. Then, s-parameters are converted to Z-parameters using

$$Z_{DUT} = 50 \frac{S_{21}}{2(1 - S_{21})} \quad (30)$$

then, M is calculated as

$$M = \frac{\Im(Z_{DUT})}{\omega} - L_1 - L_2 \quad (31)$$

where L_1 and L_2 are self-inductances of TX and RX coils. The different components of the electromagnetic field (H_x, H_z) and (E_x, E_y) for aligned coils with 10 cm air gap are depicted in Figs. 7(a) and 7(b). The measurement and numerical results of voltage signals in primary and secondary coils are displayed in Fig. 8 while the coils are aligned.

We execute numerical and experimental results for M at various positions of RX coil. The vertical distance is represented by d , and m_2 is the horizontal distance from the center of the TX coil to the center of the RX coil and angle θ represents the tilt angle between the two coils, and it is defined as the angle between the xy -plane of TX coil and xy -plane of RX coil. The shape of the electric field distribution shown in Fig. 9(a). The calculated and measured mutual inductance at various configurations are given in Fig. 9(b). The comparison among measured, analytical and DGTD results are given in Fig. 9(c). Excellent agreement was obtained between the DGTD models and both measurement and analytical results. The farther away the two coils are, the weaker the magnetic field is, and therefore, the smaller the mutual inductance will be. Fig. 10 shows the variation of the mutual inductance as a function of frequency for aligned coils. The results demonstrate that the mutual inductance between two coils intensifies

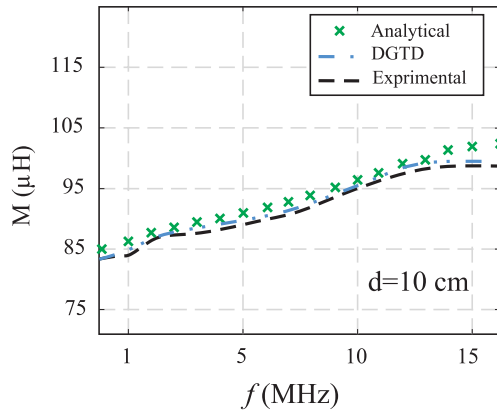


FIG. 10. Mutual inductance between two coils with distance of 12 cm at different frequencies.

as the frequency increases. In all cases, the numerical approximations are in very good agreement with the experimental results. The deviations observed at high frequencies are due to existing different error sources in measurement setups, i.e., solder joints, nonideal coil behavior, and environment effects which interfere with the measurement.

The proposed numerical technique can be applied in different types and shape of the coils. Computational costs are reasonable since the developed DGTD solver is parallelized using the Message Passing Interface (MPI) and domain decomposition techniques [46]. Domain decomposition is a family of linear algebra-based techniques. It reformulates a discrete problem into subproblems (in our case, on 8 subdomains) to distribute them on various processors of a parallel computer, and to recover the computed distributed solutions in a single global numerical approximation. This is the first study where the DGTD FEM is used for modeling WPT systems based on three-dimensional full-wave Maxwell's equations. The DGTD FEM exhibits better convergence and stability properties when compared to the standard FEM, especially for complex geometries, given the fact that equations are discretized using an element-by-element strategy, where locally computed fluxes on each element help provide stability. In addition, using Whitney elements improves numerical stability, which translates into larger time steps, and therefore in reduced computational costs. This is one of the components of the proposed numerical methodology that makes the developed solver faster than commercial codes. The developed numerical methodology is verified and validated using both analytical solutions and measurements results. For the first time, the effects of misalignment are studied with a such a high level of accuracy using numerical techniques.

V. CONCLUSION

A 3-D DGTD method for Maxwell's equations is proposed to analyze the electromagnetic behavior of WPT system. This numerical method allows to calculate the electromagnetic field propagation and mutual inductance between the two

coils and their performance against misalignment. The second order BDF time integration scheme is considered for the approximation of the time derivative in Maxwell's equations. In order to measure the influence of the basis functions, the L^2 -errors between analytical and exact numerical results are calculated for linear (P_1), and quadratic (P_2) polynomials, and Whitney basis functions. The Whitney basis function provides a good compromise between computational cost and accuracy to analyze the behavior of WPT systems. In addition to the fact that DGTD method can provide a stable discrete problem, its local nature makes it a numerical method that is easy to parallelize, which results in fast solvers for the discretization of Maxwell's equations. MPI and domain decomposition techniques are applied to dramatically improve the performance and reduce the computational time of simulations. The accuracy of the presented algorithm is assessed in comparison with the analytical and experimental results and good agreement was obtained. It is believed that the proposed method can be used for solving a large range of frequency and different geometries and it can serve as an excellent platform for the optimization of WPT in future studies.

APPENDIX A MAGNETIC FIELDS OF CIRCULAR CURRENT LOOP

The analytical solution regarding to a circular current can be calculated by [47]

$$\begin{aligned} H_x &= \frac{Cxz}{2\alpha^2\beta\rho^2} [(a^2 + r^2)E(k^2) - \alpha^2K(k^2)] \\ H_y &= \frac{Cyz}{2\alpha^2\beta\rho^2} [(a^2 + r^2)E(k^2) - \alpha^2K(k^2)] \\ H_z &= \frac{C}{2\alpha^2\beta\rho^2} [(a^2 - r^2)E(k^2) + \alpha^2K(k^2)] \end{aligned} \quad (32)$$

The following substitutions are used for simplicity: $\rho^2 = x^2 + y^2$, $r^2 = x^2 + y^2 + z^2$, $\alpha^2 = a^2 + r^2 - 2a\rho$, $\beta^2 = a^2 + r^2 + 2a\rho$, $k^2 = 1 - \alpha^2/\beta^2$, and $C = I/2\pi$. K and E represent the complete elliptic integrals of the first and the second kind, respectively.

APPENDIX B NEUMANN FORMULA DETAILS

A. ALIGNMENT

By taking advantage of symmetry at the z axis, the cylindrical coordinate system is convenient to use with this geometry. The unit vectors in the cylindrical coordinate are defined as,

$$\begin{aligned} \mathbf{e}_r &= \cos\phi \mathbf{i} + \sin\phi \mathbf{j} \\ \mathbf{e}_\phi &= -\sin\phi \mathbf{i} + \cos\phi \mathbf{j} \\ \mathbf{e}_z &= \mathbf{k} \end{aligned} \quad (33)$$

The differential length formed by considering incremental displacements dr , $r d\phi$, dz from the coordinate (r, ϕ, z) is as following,

$$d\mathbf{l} = dr \mathbf{e}_r + r d\phi \mathbf{e}_\phi + dz \mathbf{e}_z \quad (34)$$

By attention to the Ampere circuital law, the direction of magnetic field variations is around ϕ . Therefore, the differential length depends on the angle ϕ variations as following,

$$d\mathbf{l} = rd\phi \mathbf{e}_\phi \quad (35)$$

Then, from (33), (34) and (35), it can be resulted that the differential length of the conductor elements in arbitrary points of P and Q are

$$\begin{cases} d\mathbf{l}_1 = -r_1 \cos \phi_1 \mathbf{i} - r_1 \sin \phi_1 \mathbf{j} \\ d\mathbf{l}_2 = -r_2 \cos \phi_2 \mathbf{i} - r_2 \sin \phi_2 \mathbf{j} + d \mathbf{k} \end{cases} \quad (36)$$

The numerator of (18), the dot product between two vectors is calculated as,

$$d\mathbf{l}_1 \cdot d\mathbf{l}_2 = r_1 r_2 \cos(\phi_1 - \phi_2) d\phi_1 d\phi_2 \quad (37)$$

The denominator of (18), the distance between these two elements in arbitrary points of P and Q (see Fig 2 a), is calculated as,

$$r = |d\mathbf{l}_1 - d\mathbf{l}_2| = \sqrt{r_1^2 + r_2^2 - 2r_1 r_2 \cos(\phi_1 - \phi_2) + d^2} \quad (38)$$

After some simplification, by replacing (37) and (38) in (18), the mutual inductance between two circular coaxial filament coils is given in (19).

B. MISALIGNMENT

The differential length of the conductor elements in arbitrary points of P and Q (see Fig 2 b) is

$$\begin{cases} d\mathbf{l}_1 = -r_1 \cos \phi_1 \mathbf{i} - r_1 \sin \phi_1 \mathbf{j} \\ d\mathbf{l}_2 = -r_2 \cos \theta \cos \phi_2 \mathbf{i} + (-r_2 \sin \phi_2 + m_2) \mathbf{j} \\ \quad + (r_2 \sin \theta \cos \phi_2 + d) \mathbf{k} \end{cases} \quad (39)$$

The distance between these two elements in arbitrary points of P and Q is

$$r = \sqrt{(-r_1 \cos \phi_1 + r_2 \cos \theta \cos \phi_2)^2 + (-r_1 \sin \phi_1 + r_2 \sin \phi_2 - m_2)^2 + (-r_2 \sin \theta \cos \phi_2 - d)^2} \quad (40)$$

The dot product between two vectors is calculated as,

$$d\mathbf{l}_1 \cdot d\mathbf{l}_2 = r_1 r_2 (\sin \phi_1 \sin \phi_2 \cos \theta + \cos \phi_1 \cos \phi_2) d\phi_1 d\phi_2 \quad (41)$$

After some simplification, by replacing (40) and (41) in (18), the mutual inductance between two circular non-coaxial filament coils is given in (25).

REFERENCES

- [1] H. Hoang, S. Lee, Y. Kim, Y. Choi, and F. Bien, "An adaptive technique to improve wireless power transfer for consumer electronics," *IEEE Trans. Consum. Electron.*, vol. 58, no. 2, pp. 327–332, Jul. 2012.
- [2] K. Wake *et al.*, "Derivation of coupling factors for different wireless power transfer systems: Inter and intralaboratory comparison," *IEEE Trans. Electromag. Compat.*, vol. 59, no. 2, pp. 677–685, Apr. 2017.
- [3] Z. Bi *et al.*, "A review of wireless power transfer for electric vehicles: Prospects to enhance sustainable mobility," *Appl. Energy*, vol. 179, no. 1, pp. 413–425, Jul. 2016.
- [4] D. H. Tran, V. B. Vu, and W. Choi, "Design of a high efficiency wireless power transfer system with intermediate coils for the on-board chargers of electric vehicles," *IEEE Trans. Power Electron.*, vol. 33, no. 1, pp. 175–187, Feb. 2018.
- [5] Y. Bu, S. Endo, and T. Mizuno, "Improvement in the transmission efficiency of EV wireless power transfer system using a magnetoplated aluminum pipe," *IEEE Trans. Magn.*, vol. 54, no. 11, pp. 1–5, Nov. 2018.
- [6] B. Cannon, J. Hoburg, D. Stancil, and S. Goldstein, "Magnetic resonant coupling as a potential means for wireless power transfer to multiple small receivers," *IEEE Trans. Power Electron.*, vol. 24, no. 7, pp. 1819–1825, Jul. 2009.
- [7] W. Zhong, X. Liu, and S. Hui, "A novel single-layer winding array and receiver coil structure for contactless battery charging systems with free-positioning and localized charging features," *IEEE Trans. Ind. Electron.*, vol. 58, no. 9, pp. 4136–4144, Sep. 2011.
- [8] D. Ahnand and S. Hong, "Effect of coupling between multiple transmitters or multiple receivers on wireless power transfer," *IEEE Trans. Ind. Electron.*, vol. 60, no. 7, pp. 2602–2613, Jul. 2013.
- [9] C. Lu *et al.*, "Investigation of negative and near-zero permeability metamaterials for increased efficiency and reduced electromagnetic field leakage in a wireless power transfer system," *IEEE Trans. Electromag. Compat.*, vol. 61, no. 5, pp. 1438–1446, Oct. 2019.
- [10] A. Kurs, R. Moffatt, and M. Soljacic, "Simultaneous mid-range power transfer to multiple devices," *Appl. Phys. Lett.*, vol. 96, no. 4, pp. 044102-1–044102-3, Jan. 2010.
- [11] Y. Zhang, T. Lu, Z. Zhao, F. He, K. Chen, and L. Yuan, "Employing load coils for multiple loads of resonant wireless power transfer," *IEEE Trans. Power Electron.*, vol. 30, no. 11, pp. 6174–6181, Nov. 2015.
- [12] J. Kim, H. Son, D. Kim, K. Kim, and Y. Park, "Analysis of wire less energy transfer to multiple devices using CMT," *Proc. Asia-Pacific Microw. Conf., 2010*, pp. 2149–2152.
- [13] (ANSYS). [Online]. Available: <http://www.ansys.com>
- [14] COMSOL Multiphysics. [Online]. Available: <https://www.comsol.com>
- [15] *Advanced Design System (ADS)*. [Online]. Available: <https://www.keysight.com>
- [16] X. Zhang, Y. Zhao, S. L. Ho, and W. N. Fu, "Analysis of wireless power transfer system based on 3-D finite-element method including displacement current," *IEEE Trans. Magn.*, vol. 48, no. 11, pp. 3692–3695, Nov. 2012.
- [17] C.-Lin, L.-Kuo, and H.-Chuang, "A horizontally polarized omnidirectional printed antenna for WLAN applications," *IEEE Trans. Antennas Propag.*, vol. 54, no. 11, pp. 3551–3556, Nov. 2006.
- [18] K. Michal, E. Cherkav, and P. Wannamaker, "Variational formulation for maxwell's equations with lorenz gauge: Existence and uniqueness of solution," *Int. J. Numer. Anal. Model.*, vol. 12, no. 4, pp. 731–749, 2015.
- [19] S. Park, "Evaluation of electromagnetic exposure during 85 kHz wireless power transfer for electric vehicles," *IEEE Trans. Magn.*, vol. 54, no. 1, pp. 1–8, Jan. 2018.
- [20] S. W. Park, K. Wake, and S. Watanabe, "Incident electric field effect and numerical dosimetry for a wireless power transfer system using magnetically coupled resonances," *IEEE Trans. Microw. Theory Technol.*, vol. 61, no. 9, pp. 3461–3469, Sep. 2013.
- [21] H. Xu, D. Ding, J. Bi, and R. Chen, "A 3-D continuous discontinuous galerkin finite-element time-domain method for maxwell's equations," *IEEE Antennas Wireless Propag. Lett.*, vol. 16, pp. 908–911, 2017.
- [22] S. D. Gedney, J. C. Young, T. C. Kramer, and J. A. Roden, "A discontinuous galerkin finite element time-domain method modeling of dispersive media," *IEEE Trans. Antennas Propag.*, vol. 60, no. 4, pp. 1969–1977, Apr. 2012.
- [23] J. Chen, Q. H. Liu, M. Chai, and J. A. Mix, "A nonspurious 3-D vector discontinuous galerkin finite-element time-domain method," *IEEE Microw. Wireless Compon. Lett.*, vol. 20, no. 1, pp. 1–3, Jan. 2010.
- [24] J. S. Hesthaven and T. Warburton, *Nodal Discontinuous Galerkin Methods: Algorithms, Analysis, and Applications*. Springer, 2007.
- [25] C. Bernardi and Y. Maday, "Polynomial interpolation results in sobolev spaces," *J. Comput. Appl. Math.* 43, pp. 53–80, 1992.
- [26] C. Geuzaine and J.-F. Remacle, "GMSH: A three-dimensional finite element mesh generator with built-in pre- and post-processing facilities," *Int. J. Numer. Methods Eng.* vol. 79, no. 11, pp. 1309–1331, 2009.
- [27] A. Logg, K.-A. Mardal, and G. Wells, *Automated Solution of Differential Equations by the Finite Element Method*, Springer, 2012, doi: 10.1007/978-3-642-23099-8.

- [28] H. Gao, "Unconditional optimal error estimates of BDF-Galerkin FEMs for nonlinear thermistor equations," *J. Sci. Comput.*, vol. 66, pp. 504–527, 2016. [Online]. Available: <https://doi.org/10.1007/s10915-015-0032-5>
- [29] V. Zuijlen, H. Alexander, and B. Hester, "Implicit and explicit higher order time integration schemes for structural dynamics and fluid-structure interaction computations," *Elsevier Comput. Structures*, vol. 83, no. 2-3, pp. 93–105, 2005.
- [30] J. C. Maxwell, *A Treatise on Electricity and Magnetism*. New York, NY, USA: Dover, vol. 2.
- [31] S. I. Babic *et al.*, "Validity check of mutual inductance formulas for circular filaments with lateral and angular misalignments," *Progress Electromagnetics Res. M.*, vol. 8, pp. 15–26, 2009.
- [32] S. Butterworth, "On the coefficients of mutual induction of eccentric coils," *Phil. Mag., Ser. 6*, 31, pp. 443–454, 1916.
- [33] C. Snow, "Formulas for computing capacitance and inductance," *Nat. Bur. Standards Circular 544*, Washington DC, Dec. 1954.
- [34] F. W. Grover, *Inductance Calculation: Working Formulas and Tables*. New York, NY, USA: Dover, 1946.
- [35] S. Babic and C. Akyel, "Magnetic force between inclined circular filaments placed in any desired position," *IEEE Trans. Magn.*, vol. 48, no. 1, pp. 69–80, Jan. 2012.
- [36] P. L. Kalantarov *Inductance Calculations*. Moscow, Russia: National Power Press, 1955.
- [37] S. Ramo, J. R. Whinnery, T. V. Duzer, *Fields and Waves in Communication Electronics*. Hoboken, NJ, USA: John Wiley and Sons Inc., 1994.
- [38] M. Bagheri, S. Nezhivenko, B. T. Phung, and T. Blackburn, "Air core transformer winding disk deformation: A precise study on mutual inductance variation and its influence on frequency response spectrum," *IEEE Access*, vol. 6, pp. 7476–7488, 2018.
- [39] Z. Li and J. Yi, "Modeling and design of a transmission coil and four cascaded receiving coils wireless charging structure with lateral misalignments," *IEEE Access*, vol. 8, pp. 75976–75985, 2020.
- [40] S. R. Khan, S. K. Pavuluri, and M. P. Y. Desmulliez, "Accurate modeling of coil inductance for near-field wireless power transfer," *IEEE Trans. Microw. Theory Techn.*, vol. 66, no. 9, pp. 4158–4169, Sep. 2018.
- [41] B. Arabsalmanabadi, H. Arab, S. Dufour, and K. Al-Haddad, "Analytical and numerical design study of torus coils with misalignment for efficient inductive energy transmission in EV chargers," *Proc. IECON IEEE 45th Annu. Conf. Ind. Electron. Soc.*, 2019, pp. 2622–2627.
- [42] Z. H. Shi, X. Y. Chen, and Z. C. Qiu, "Modeling of mutual inductance between superconducting pancake coils used in wireless power transfer (WPT) systems," *IEEE Trans. Appl. Supercond.*, vol. 29, no. 2, pp. 1–4, Mar. 2019.
- [43] L. Qian, M. Chen, K. Cui, G. Shi, J. Wang, and Y. Xia, "Modeling of mutual inductance between two misalignment planar coils in wireless power transfer," *IEEE Microw. Wireless Compon. Lett.*, vol. 30, no. 8, pp. 814–817, Aug. 2020.
- [44] A. Pacini, A. Costanzo, S. Aldhaher, and P. D. Mitcheson, "Load- and position-independent moving MHz WPT system based on GaN-Distributed current sources," *IEEE Trans. Microw. Theory Techn.*, vol. 65, no. 12, pp. 5367–5376, Dec. 2017.
- [45] U. Ayachit, "The ParaView guide: A parallel visualization application," Kitware, 2015.
- [46] B. Barney, "Message passing interface (MPI)," in *Encyclopedia of Parallel Computing*, D. Padua, ed., pp. 1116–1116, Boston, MA, US: Springer, 2011.
- [47] R. A. Schill, "General relation for the vector magnetic field of a circular current loop," *IEEE Trans. Magn.*, vol. 39, no. 2, pp. 961–967, Mar. 2003.